Low Cloud–SST Variability over the Summertime Subtropical Northeast Pacific: Role of Extratropical Atmospheric Modes⬨

AYUMU MIYAMOTO ⬤[a] AND SHANG-PING XIE[a]

[a] *Scripps Institution of Oceanography, University of California San Diego, La Jolla, California*

ABSTRACT: Over the subtropical Northeast Pacific (NEP), highly reflective low clouds interact with underlying sea surface temperature (SST) to constitute a local positive feedback. Recent modeling studies showed that, together with wind–evaporation–SST (WES) feedback, the summertime low cloud–SST feedback promotes nonlocal trade wind variations, modulating subsequent evolution of El Niño–Southern Oscillation (ENSO). This study aims to identify drivers of summertime low-cloud variations, using satellite observations and global atmosphere model simulations forced with observed SST. A transbasin teleconnection is identified, where the north tropical Atlantic (NTA) warming induced by the North Atlantic Oscillation (NAO) increases precipitation, exciting warm Rossby waves that extend into the NEP. The resultant enhancement of static stability promotes summertime low cloud–SST variability. By regressing out the effects of the preceding ENSO and NTA SST, atmospheric internal variability over the extratropical North Pacific, including the North Pacific Oscillation (NPO), is found to drive the NEP cooling by latent heat loss and subsequent summer low cloud–SST variability. With the help of the background trade winds and WES feedback, the SST anomalies extend southwestward from the low-cloud region, accompanied by ENSO in the following winter. This suggests the nonlocal effects of low clouds identified by recent studies. Analysis of a 500-yr climate model simulation corroborates the NTA and NPO forcing of NEP low cloud–SST variability and subsequent ENSO.

KEYWORDS: Pacific Ocean; Subtropics; Clouds; ENSO; Air–sea interaction

1. Introduction

The subtropical Northeast Pacific (NEP) is frequently covered by low-level clouds of tops at 1–2 km above the sea surface (Fig. 1a; Wood 2012). Reflecting insolation strongly, these clouds are important in local and global radiation budgets (Hartmann and Short 1980). Lower-tropospheric stability associated with subtropical subsidence and low sea surface temperature (SST) favors low clouds (Fig. 1a; Klein and Hartmann 1993; Wood and Bretherton 2006; Koshiro and Shiotani 2014). This constitutes a positive feedback loop, in which SST cooling by low clouds promotes more low-cloud formation. This low cloud–SST feedback is crucial in interannual SST variations over the NEP (Norris and Leovy 1994; Norris et al. 1998; Clement et al. 2009; Myers et al. 2018; Myers and Mechoso 2020; Yang et al. 2023).

The North Pacific meridional mode (NPMM; Chiang and Vimont 2004) is a recurrent pattern of interannual variability due to wind–evaporation–SST (WES) feedback (Xie and Philander 1994). An anomalous SST cooling in the NEP induces a surface anticyclone to the west that strengthens the trade winds. The resultant evaporative cooling reinforces the SST cooling, causing the coupled SST–wind pattern to propagate southwestward. This NPMM acts as a conduit for extratropical/subtropical variability to affect the equatorial Pacific (e.g.,

Chang et al. 2007; Ma et al. 2017; Luongo et al. 2023). In particular, the NPMM is recognized as a precursor of the El Niño–Southern Oscillation (ENSO), the dominant mode of interannual variability in the global climate system. Extending from the NEP into the deep tropics, the NPMM generates equatorial zonal wind anomalies through the WES feedback and summer deep convection response (Amaya 2019). These equatorial winds trigger the ENSO in the subsequent winter through the Bjerknes feedback (Bjerknes 1969).

Low cloud–SST feedback has traditionally been considered local to the NEP low-cloud region, but localized SST anomalies over the NEP induce atmospheric circulation response, thereby activating the WES feedback and NPMM-like coupled response (Bellomo et al. 2014; Middlemas et al. 2019; Yang et al. 2023; Miyamoto et al. 2023). The fact that the NPMM has a large SST loading under the NEP low-cloud deck is suggestive of the role of the joint low cloud–WES feedback in energizing the NPMM (Xie 2024). Indeed, the NPMM and its impact on the ENSO both diminish when the cloud–SST coupling is disabled in a global climate model (so-called cloud-locking simulation; Yang et al. 2023).

Trade wind variability associated with the wintertime North Pacific Oscillation (NPO; Walker and Bliss 1932; Rogers 1981) is an important driver of the NPMM through the WES-type seasonal footprinting mechanism (Vimont et al. 2003; Chiang and Vimont 2004; Zhang et al. 2021, 2022). Springtime SST variability over the north tropical Atlantic (NTA), by inducing low-level wind anomalies over the NEP, is an additional mechanism for the NPMM (Ham et al. 2013; Rodríguez-Fonseca et al. 2020; Kug et al. 2020; Ma et al. 2021; Yang et al. 2022). While summertime low-cloud variability over the NEP is associated with coherent concurrent SST and surface wind anomalies

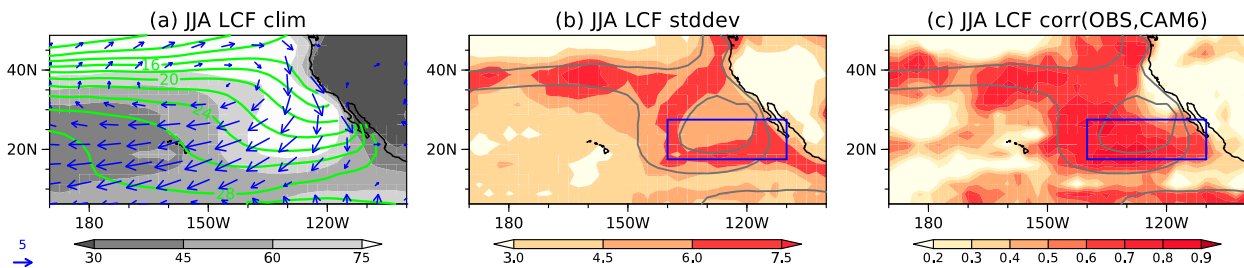*Corresponding author*: Ayumu Miyamoto, aymiyamoto@ucsd.edu

FIG. 1. JJA climatology and interannual variability of LCF. (a) Climatological distribution of MODIS LCF (%; shading). Superimposed with green contours and blue arrows are climatological-mean ERSST SST (contoured for every 2°C) and ERA5 surface winds (m s^{-1}; arrows with reference on the left), respectively. (b) Interannual standard deviation of MODIS LCF (%; color shading). (c) Interannual correlation between MODIS and CAM6-AMIP LCF. In (b) and (c), the 60% and 80% lines of climatological-mean MODIS LCF are superimposed. Blue box denotes the NEP box. See section 2 for details of the data.

(Klein et al. 1995; Norris et al. 1998), the drivers such as the NPO and NTA SST remain to be systematically investigated.

This study aims to reveal drivers of summertime low-cloud variability over the NEP, using satellite observations of cloud and radiation available in homogeneous global coverage from 2000. A multiple linear regression framework is introduced to disentangle the effects of the ENSO, interbasin teleconnection from the NTA, and North Pacific stochastic variability. Contributions from SST forcing and atmospheric internal variability are inferred using atmosphere general circulation models (AGCMs) forced with observed SST, following the Atmospheric Model Intercomparison Project (AMIP) protocol. We will investigate low cloud–SST variability over the NEP and its impact on the NPMM and subsequent ENSO behavior. The limited observational record is complemented by a 500-yr fully coupled simulation of the Community Earth System Model, version 2 (CESM2; Danabasoglu et al. 2020).

The rest of the paper is organized as follows. Section 2 describes the data used in this study. Section 3 examines lagged relationship with the ENSO and NTA SST and introduces our multiple linear regression framework. Based on the multiple linear regression, section 4 identifies the NTA forcing on the NEP low clouds. Similarly, section 5 reveals stochastic forcing over the North Pacific. Section 6 discusses nonlocal low-cloud feedback on the NPMM and subsequent ENSO and supports from the CESM2 simulation. Section 7 summarizes the present study.

2. Data

a. Observational datasets

We use satellite observations of cloud and radiation from March 2000 through December 2021. We calculate low-cloud fraction (LCF) from 1° cloud product collection 6.1 of the Moderate Resolution Imaging Spectroradiometer (MODIS) on board Terra (Platnick et al. 2015). Low clouds are defined as those with cloud-top pressure greater than 680 hPa. Since passive measurements cannot detect low clouds covered by middle or high clouds, the presence of these clouds may underestimate LCF. To circumvent the spurious LCF decrease, we apply the random overlap assumption:

$$LCF_r = LCF/(1 - MHCF), \qquad (1)$$

where LCF is monthly mean low-cloud fraction and MHCF is the sum of middle- and high-cloud fractions. The validity of the assumption is discussed in Warren et al. (1988) and Norris (2005). The rest of the analysis utilizes LCF$_r$ as true LCF. For radiative fluxes, we use the Clouds and the Earth's Radiant Energy System (CERES) Energy Balanced and Filled (EBAF) edition 4.2 (Loeb et al. 2018; Kato et al. 2018) on a 1° grid.

We also use Extended Reconstructed SST (ERSST; Huang et al. 2017), version 5, for SST and Objectively Analyzed Air–Sea Fluxes (OAFlux; Yu and Weller 2007), version 3, for turbulent heat fluxes. For precipitation, we use the Global Precipitation Climatology Project (GPCP; Huffman et al. 2023), version 3.2. For other meteorological fields, we use the ERA5 global atmospheric reanalysis (Hersbach et al. 2020). These datasets cover the period of the MODIS and CERES observations. Finally, monthly climatology of ocean mixed-layer depth is estimated from the Mixed Layer Dataset of Argo, Grid Point Value (MILA-GPV; Hosoda et al. 2010) for the 2001–22 period. As in CESM2, we use the mixed-layer depth defined as the depth at which potential density difference is 0.03 kg m^{-3} relative to the surface. The horizontal resolution is 2° in ERSST, 0.5° in GPCP, and 1° in OAFlux, ERA5, and MILA-GPV.

b. AMIP simulations

We utilize a 10-member AMIP ensemble with the Community Atmosphere Model, version 6 (CAM6; Danabasoglu et al. 2020), from March 2000 through December 2021 (CAM6-AMIP. CAM6 is the atmospheric component of CESM2 with a nominal 1° horizontal resolution and 32 vertical levels. CAM6-AMIP is radiatively forced with historical (until 2014) and shared socioeconomic pathway (SSP3-7.0) scenarios from phase 6 of the Coupled Model Intercomparison Project (CMIP6; Eyring et al. 2016). Prescribed SST and sea ice are ERSST.v5 and Hadley Centre Ice and SST, version 1 (HadISST1; Rayner et al. 2003), respectively. We analyze the ensemble average to assess SST effect in the observational record. If the AMIP simulation fails to reproduce an observed anomaly, the anomaly can be regarded as stochastic variability of the atmosphere. Although the decoupling of the ocean can weaken the variance of atmospheric teleconnection patterns in AMIP, this effect is generally small (around 10% at most; Mori et al. 2024).

c. Sensitivity experiments with Atlantic SST

To test the NTA influence, we conduct a set of AGCM experiments with GFDL Atmospheric Model, version 2.1 (AM2.1) (GFDL Global Atmospheric Model Development Team 2004). AM2.1 has 2.5° × 2° resolution in longitude–latitude with 24 vertical levels. Although AM2.1 does not reproduce low-cloud variability as well as CAM6, the responses of large-scale circulation and precipitation in AM2.1 are nearly identical to those in CAM6. As in CAM6-AMIP, a control experiment (AM2.1-AMIP) is run with ERSST.v5 (Huang et al. 2017) from 2000 to 2021 under historical radiative forcing until 2005 and representative concentration pathway (RCP) 4.5 afterward (Taylor et al. 2012). In a sensitivity experiment (AM2.1-ATL), we set monthly climatology of SST outside the Atlantic Ocean (33°S–63°N) so that only the Atlantic SST varies interannually. Either experiment has 10 ensemble members, all of which are averaged to discuss the NTA SST effect.

d. Preindustrial simulations

We also utilize a 500-yr fully coupled simulation with CESM2 under radiative forcing fixed at the preindustrial level (CESM2-PI). This climate model is CAM6 coupled with a nominal 1° ocean model with 60 vertical levels. As in the observational analysis, we assess SST forcing in CESM2-PI using a 1-member perfect SST AMIP simulation with CAM6 (CAM6-PI). CAM6-PI is forced with daily SST and sea ice from CESM2-PI during the same period.

e. Preprocessing and statistical test

We interpolated all the data onto a 2.5° grid. Anomalies are defined as deviations from monthly climatology after detrended. The statistical significance of correlation and regression coefficient is determined with a Student's t test. The degree of freedom is estimated following Metz (1991). Effective decorrelation time T_e is estimated as follows:

$$T_e = 1 + 2 \sum_{\tau=1}^{L} \left(1 - \frac{\tau}{L}\right) R_{XX}(\tau) R_{YY}(\tau). \quad (2)$$

The terms $R_{XX}(\tau)$ and $R_{YY}(\tau)$ indicate autocorrelation function of variables X and Y at a lag of τ years. The L is taken as 10 years. In multiple linear regression, we calculate decorrelation time of a variable with individual predictors and use the largest one. Effective sample number N_e becomes

$$N_e = \frac{N}{T_e}, \quad (3)$$

where N is the number of samples.

3. Disentangling ENSO and NTA forcings

a. NEP low cloud–ENSO relationship

This section gives an overview of NEP low-cloud variations. Figure 1b shows interannual standard deviation of LCF in summer. It features strong LCF variability in the low-cloud region, especially on the southern flank, as found in previous
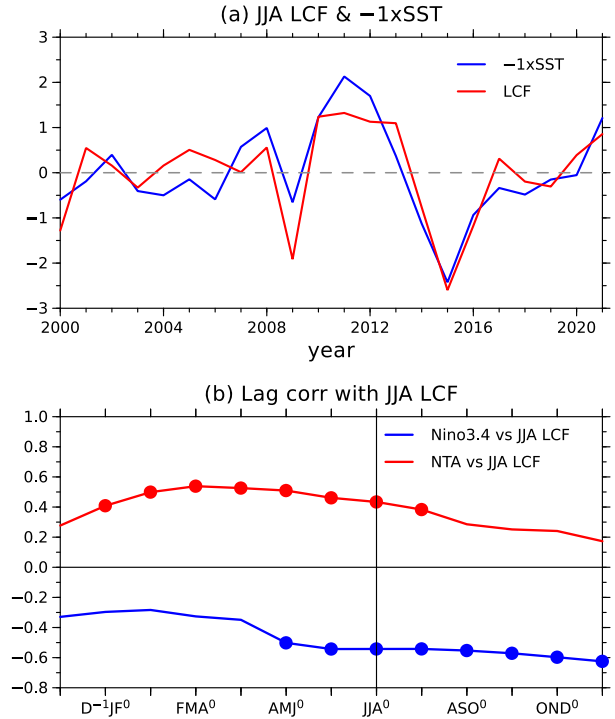

FIG. 2. Time series and lag correlation of JJA LCF averaged in the NEP box (black box in Fig. 1). (a) Normalized time series of JJA^0 MODIS LCF (red) and ERSST SST multiplied by −1 (blue) in the NEP box. (b) Lag correlation of the 3-month-mean Niño-3.4 (blue) and NTA (red) indices with JJA^0 LCF in the NEP box. Dot signifies the 90% confidence.

studies (Klein et al. 1995; Yang et al. 2023). Time series of JJA LCF averaged in the NEP box (17.5°–27.5°N, 140°–110°W) correlates well with local SST ($r = -0.83$), with enhanced variability after 2005 (Fig. 2a). The ensemble average of CAM6-AMIP successfully captures the NEP LCF variability with a maximum correlation of about 0.8. CAM6's high skill in reproducing low-cloud variability also indicates the importance of SST forcing.

Yang et al. (2023) pointed out that summertime variations of the NEP SST and low clouds correlate with antecedent and subsequent ENSO events. Blue line in Fig. 2b shows lag correlation of the Niño-3.4 index with JJA LCF in the NEP box (red line in Fig. 2a). Hereafter, superscript numerals indicate the preceding (−1), present (0), and following (1) years. The summer low-cloud increase is concomitant with a La Niña that seemingly lasts from the previous to following winters (Fig. 2b). Regressed anomalies against the Niño-3.4 index in ND^{-1}J^0, which is the peak season of the ENSO (Deser et al. 2010), feature SST warming and low-cloud decrease in the NEP, accompanied by NPMM-like warmed SST and weakened trade winds to the southwest in summer (Fig. S1 in the online supplemental material). Note that the slight difference in the location of the ENSO-induced LCF anomalies leads to the modest correlation between preceding Niño-3.4 index and JJA^0 LCF in the NEP box. While the negative correlation continues until subsequent winter, the majority of ENSO
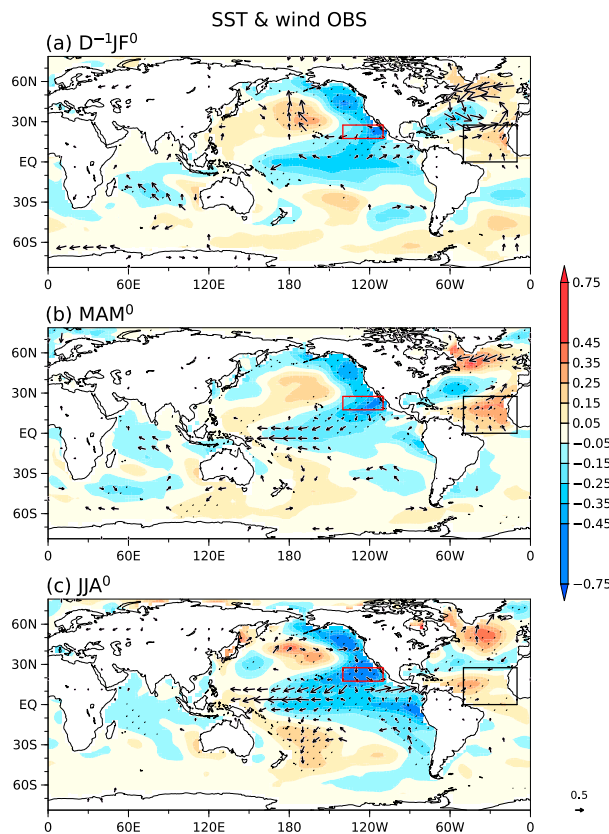
FIG. 3. (a)–(c) Lagged regression coefficients of SST (°C; color shading) and surface winds (m s^{-1}; arrows) onto JJA^0 LCF averaged in the NEP box in (a) D^{-1}JF^0, (b) MAM^0, and (c) JJA^0. Stippling indicates above 90% significance levels for the color-shaded variables, and wind arrows are drawn only if exceeding 90% significance level. The NEP (red) and NTA (black) boxes are highlighted.

events, especially El Niño, are single-year events (Okumura and Deser 2010). The ENSO signal almost vanishes in boreal summer (Fig. S1) and remains neutral in the following winter (figure not shown). Although this does not necessarily rule out the association of low-cloud variations with 2-yr ENSO events, the summer low-cloud variations accompanied by the subsequent ENSO demand other mechanisms.

The NTA SST forcing is a candidate. Figure 3 shows global distributions of SST and surface wind anomalies regressed onto JJA LCF over the NEP box, and red line in Fig. 2b shows lag correlation of SST averaged in the NTA (0°–20°N, 50°–10°W) (hereafter NTA index). The most prominent signal is positive SST anomaly in the NTA that peaks in spring. This signal is unlikely to be forced by the ENSO, as the preceding La Niña acts to produce an NTA cooling through atmospheric teleconnections (Alexander et al. 2002). We therefore hypothesize that the spring NTA warming acts to increase the summertime NEP low clouds.

b. Multiple linear regression

Considering the preceding ENSO effects on the Northeast Pacific low clouds, SST, and winds, we introduce a multiple linear regression framework using the ND^{-1}J^0 Niño-3.4 and MAM^0 NTA indices as predictors to better extract the NTA influence. Such a framework has been used to discuss the NTA influence on the ENSO (Ham et al. 2013; Ham and Kug 2015). A field variable $P(\mathbf{x}, t)$, e.g., LCF and SST, is expressed as

$$P(\mathbf{x}, t) = \alpha(\mathbf{x}, t) \times \text{N}^{-1}\text{DJ}^0 \text{ Niño 3.4} + \beta(\mathbf{x}, t)$$
$$\times \text{MAM}^0 \text{ NTA} + \text{residual}, \qquad (4)$$

where $\alpha(\mathbf{x}, t)$ and $\beta(\mathbf{x}, t)$ are partial regression coefficients onto normalized ND^{-1}J^0 Niño 3.4 and MAM^0 NTA indices, respectively. The correlation between the predictors is 0.34, as the preceding El Niño produces the NTA warming through atmospheric teleconnections (Alexander et al. 2002). Using $\beta(\mathbf{x}, t)$ in (4), section 4 reveals the NTA influence on the NEP low-cloud variations.

Figure 4 examines the correlation of the multiple linear regression estimates with observations. For summer LCF, the correlation amounts to 0.4–0.7 over the NEP low-cloud region (Fig. 4a). The regression analysis well explains summertime SST variations in not only the NEP low-cloud region but also the downstream trade wind region (Fig. 4b), suggestive of joint low cloud–WES feedback. Still, more than 50% variance of NEP LCF and SST is unexplained by the preceding ENSO and NTA SST. The residual component of the multiple linear regression analysis will be discussed in section 5.
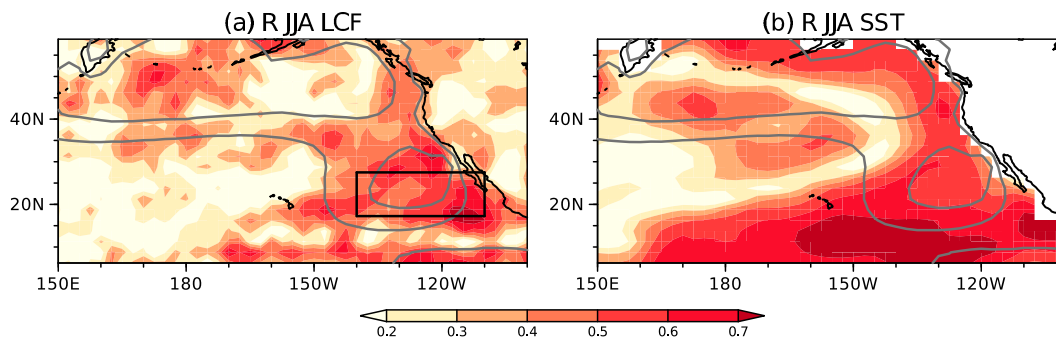

FIG. 4. JJA correlation of (a) LCF and (b) SST estimated by the multiple regression (4) with observations. The 60% and 80% lines of climatological-mean MODIS LCF are superimposed.
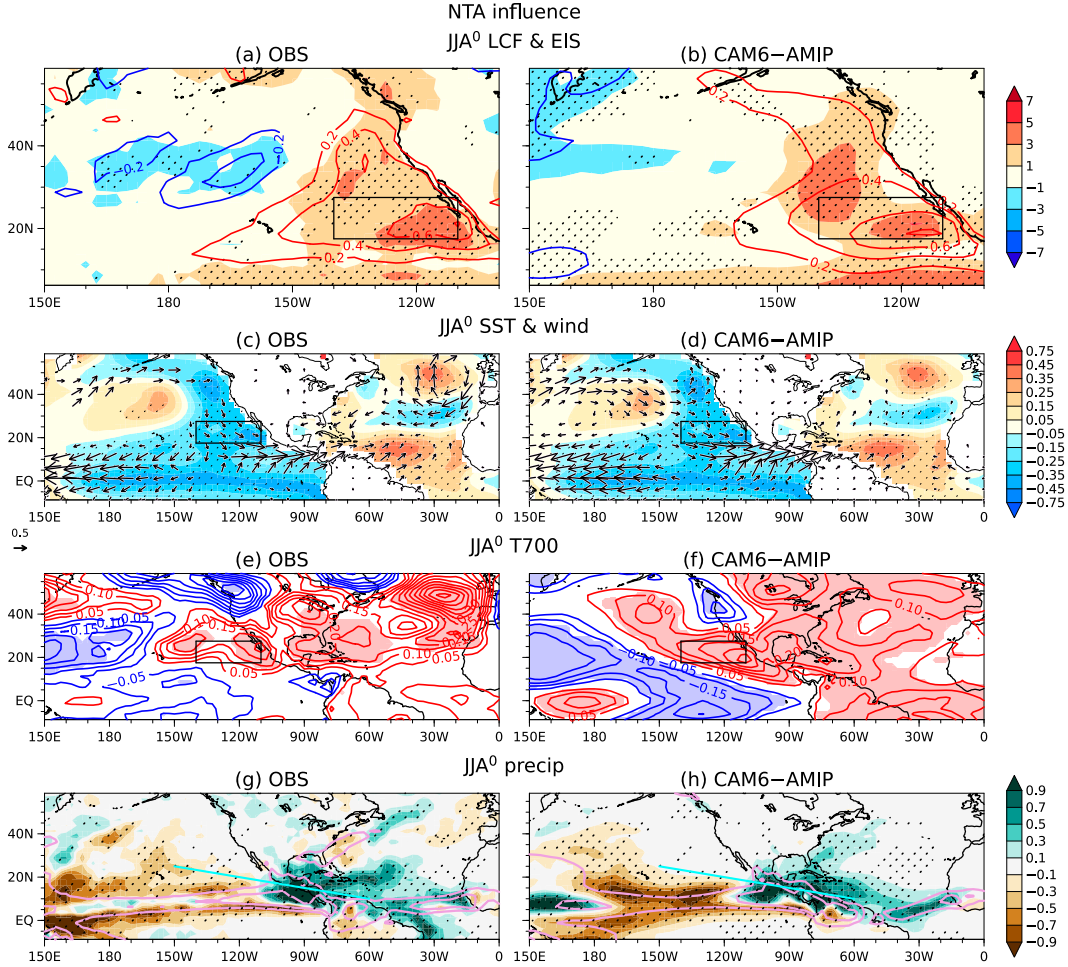
FIG. 5. JJA^0 partial regression coefficients onto the MAM^0 NTA index in (a),(c),(e),(g) observations and (b),(d),(f),(h) CAM6-AMIP. (a),(b) LCF (%; color shading) and EIS (contoured from every 0.2 K with zero lines omitted). (c),(d) SST (°C; color shading) and surface winds (m s^{-1}; arrows; only points with the 90% confidence are drawn). (e),(f) The 700-hPa temperature (contoured for every 0.05 K with zero lines omitted; color shading signifies the 90% confidence). (g),(h) Precipitation (mm day^{-1}; color shading). Superimposed with purple lines are climatological-mean precipitation (5 and 10 mm day^{-1}). Except for (e) and (f), stippling signifies the 90% confidence for the color-shaded variables. Black box in (a)–(f) denote the NEP box. Light blue line in (g) and (h) indicates cross section in Fig. 7.

4. Transbasin influence from the North Tropical Atlantic

a. Influence on NEP low clouds

First, we discuss the NTA influence on the NEP LCF based on partial regression onto the MAM^0 NTA index, $\beta(\mathbf{x}, t)$. Figure 5a indicates summertime LCF anomalies associated with the NTA warming. It features positive anomalies over the NEP with a peak around 20°N. These anomalies are collocated with the negative SST anomalies (Fig. 5b), suggestive of positive low cloud–SST feedback. Estimated inversion strength (EIS; Wood and Bretherton 2006), which is a measure of lower-tropospheric stability (i.e., potential temperature difference between the surface and 700-hPa levels), explains the low-cloud increase due partly to the SST cooling (Fig. 5a).

Comparison of surface latent heat and radiative fluxes highlights the importance of low cloud–SST feedback on the NEP SST cooling. As anomalous latent heat flux is a mixture of atmosphere-driven and SST-driven components, we estimate the latter following the bulk formula and approximate the former as residual (Du and Xie 2008; Xie et al. 2010; Miyamoto et al. 2023). Anomalous SST-driven flux (F'^{o}_{LH}) may be cast as

$$F'^{o}_{LH} = \overline{F_{LH}}\left(\frac{1}{q_s}\frac{dq_s}{dT}\right)SST', \qquad (5)$$

where T and q_s are temperature and saturation specific humidity following the Clausius–Clapeyron equation, respectively. Overbar and prime denote monthly climatology and anomaly, respectively. The residual of anomalous latent heat

flux represents the atmosphere-driven component ($F_{LH}^{a'}$) related to anomalous atmospheric conditions (wind speed, relative humidity, and difference between SST and surface air temperature):

$$F_{LH}^{a'} = F_{LH}' - F_{LH}^{o'}. \qquad (6)$$

After dividing the surface fluxes by seawater density ($\rho = 1026$ kg m^{-3}), specific heat ($c_p = 3990$ J kg °C), and monthly climatology of ocean mixed-layer depth ($\overline{H}$), we compare time tendency of ocean-mixed layer temperature (i.e., SST tendency) induced by radiative flux (shortwave and longwave components; F_{SW+LW}') and atmosphere-driven latent heat flux. We note that summertime decrease of climatological mixed-layer depth ($\overline{H}$) amplifies anomalous surface flux effect (Fig. S2).

Figure 6a shows time series of SST tendency by F_{SW+LW}' and $F_{LH}^{a'}$ along with the evolution of the SST anomaly in the NEP box. Although Ham et al. (2013) focused on evaporative cooling, low-cloud radiative cooling plays a more important role in the NEP SST anomaly peaking in late summer. The dominance of the low-cloud cooling is well captured by CAM6-AMIP prescribed with observed SST (Figs. 5b and 6b), corroborating positive low cloud–SST feedback.

Then, how does the NTA warming promote the low cloud–SST feedback over the NEP? In addition to the preceding SST cooling, we find the effect of tropospheric warming. Figure 5e shows 700-hPa temperature anomalies. Free-tropospheric warming intrudes into the NEP from the Gulf of Mexico. The cross section along the warming signal reveals its deep structure, which overlies the cooled boundary layer reflecting SST underneath (Fig. 7a). Temperature anomaly at sea surface and 700-hPa levels in the NEP box is −0.29 and +0.15 K (+0.21 K in CAM6-AMIP; Fig. 5f), respectively, although part of the SST anomaly is induced by low cloud–SST feedback due to free-tropospheric warming. This warming enhances lower-tropospheric stability together with the NEP SST cooling. The deep tropospheric warming associated with downward motions over the NEP and upward motions over the NTA (Fig. 7a) can be regarded as a baroclinic Rossby wave response (Matsuno 1966; Gill 1980) to increased convective heating induced by the NTA warming (Fig. 5g). Such a Rossby wave response accompanied by cyclonic surface wind anomalies (Fig. 5c) has already been identified in previous studies (Ham et al. 2013; Ma et al. 2021), but here we highlight the importance of free-tropospheric warming in driving coupled low cloud–SST anomalies. The Rossby wave pattern induced by the NTA warming is also found in the CAM6-AMIP simulation (Figs. 5d,f,h and 7b), corroborating the NTA forcing on NEP low clouds.

The dominance of the NTA forcing is substantiated by our additional AGCM experiments with GFDL AM2.1. Figures 8b and 8e show partial regression onto the NTA index in (4) in AM2.1-AMIP. AM2.1-AMIP well reproduces the enhanced precipitation in the western tropical Atlantic and adjacent continents as in the observations (Figs. 8a,d). Despite the overestimated warming over Mexico, it induces free-tropospheric warming and anomalous surface cyclone extending into the NEP as warm (downwelling) Rossby waves (Figs. 8a,b,d,e). These
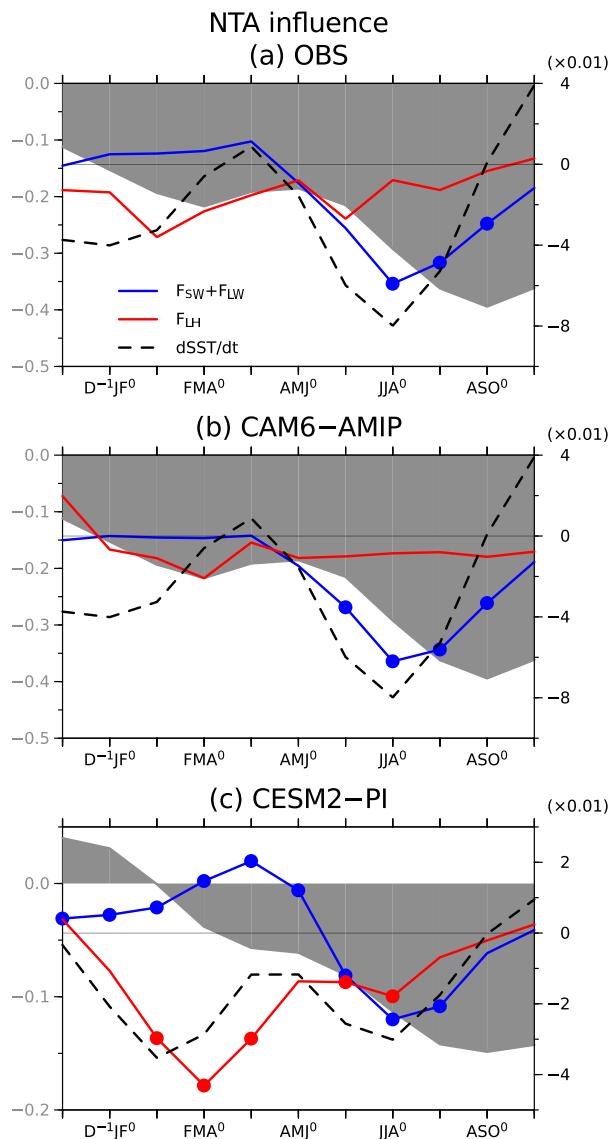

FIG. 6. Lagged regression of surface radiation and latent heat flux due to the NTA SST warming. The 3-month-mean partial regression coefficients of $F_{SW+LW}'/\rho c_p \overline{H}$ (blue) and $F_{LH}^{a'}/\rho c_p \overline{H}$ (red) in the NEP box onto the MAM^0 NTA index in (a) observations, (b) CAM6-AMIP, and (c) CESM2-PI. Unit is °C (30 day)$^{-1}$ with reference on the right axis. Dot signifies the (a) and (b) 90% and (c) 99% confidence. Gray filled line and black dotted line indicate the corresponding partial regression of SST (°C; reference on the left axis) and its time derivative [°C (30 day)$^{-1}$] averaged over the NEP box, respectively, in (a) and (b) observations and (c) CESM2-PI.

responses resemble those in CAM6-AMIP (Fig. 5). As shown in Figs. 8c and 8f, AM2.1-ATL mostly captures the Rossby waves, which substantiates the dominance of the NTA SST effect. In summary, the NTA warming excites free-tropospheric warming and hence promotes summertime LCF increase and SST cooling over the NEP.
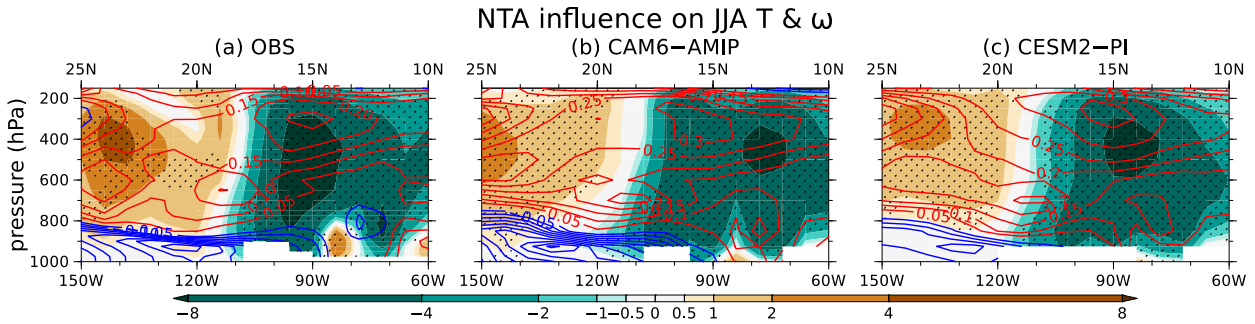
NTA influence on JJA T & ω

FIG. 7. Northwest–southeast vertical cross section between (25°N, 150°W) and (10°N, 60°W) along light blue line in Figs. 5g,h and 15. JJA^0 partial regression of ω (hPa day^{-1}; color shading) and temperature (every 0.05 K; zero lines omitted) onto the MAM^0 NTA index in (a) observations, (b) CAM6-AMIP, and (c) CESM2-PI. Dot signifies the (a) and (b) 90% and (c) 99% confidence for ω.

b. Stochastic NAO forcing via NTA warming

Lag regression analysis identifies stochastic forcing on NEP low clouds via the NTA warming. Figure 9 shows lagged partial regression of SST and wind with respect to the NTA warming. In spring, the NTA warming is collocated with reduced trade wind (Fig. 9a) similar to the Atlantic meridional mode (Xie and Carton 2004; Chiang and Vimont 2004). Considering the delay of the ocean response to atmospheric forcing, we examine the preceding sea level pressure (SLP) anomalies in FMA^0. Figure 10a features a meridional dipole known as the negative North Atlantic Oscillation (NAO; Walker and Bliss 1932; Wallace and Gutzler 1981), which weakens the trade winds and kicks off the Atlantic meridional mode (Chang et al. 2001). The SST-forced SLP anomalies assessed with CAM6-AMIP do not compare well with this pattern (Fig. 10b), indicating that this NAO is mostly the atmospheric internal variability. Despite a weak hint of the NAO, AM2.1-AMIP also fails to reproduce the observed NAO signal (Fig. S3). The NAO-induced NTA SST anomalies persist through summer (Fig. 9b), intensifying deep convection

over the western tropical Atlantic and adjacent continents (Fig. 5g) to promote low cloud–SST variability over the NEP (Fig. 5a). Qualitatively similar results can be obtained when the MAM^0 NTA index is replaced by the FMA^0 NAO index (Fig. S4). Thus, this study has for the first time identified the NAO influence on NEP low clouds.

5. Stochastic NPO forcing

The multiple linear regression analysis enables us to define a residual component that is uncorrelated with either the preceding $ND^{-1}J^0$ Niño-3.4 or MAM^0 NTA index. By using the residual component, we perform simple regression analysis onto normalized JJA^0 MODIS LCF averaged in the NEP box (residual LCF index). Our multiple linear regression analysis does not distinguish the central Pacific (CP) and eastern Pacific (EP) types of ENSO. This leaves a possibility that the ENSO flavors might be important in the residual components. As we will see, however, the residual low-cloud variability highlights low cloud–SST feedback triggered by midlatitude stochastic variability.
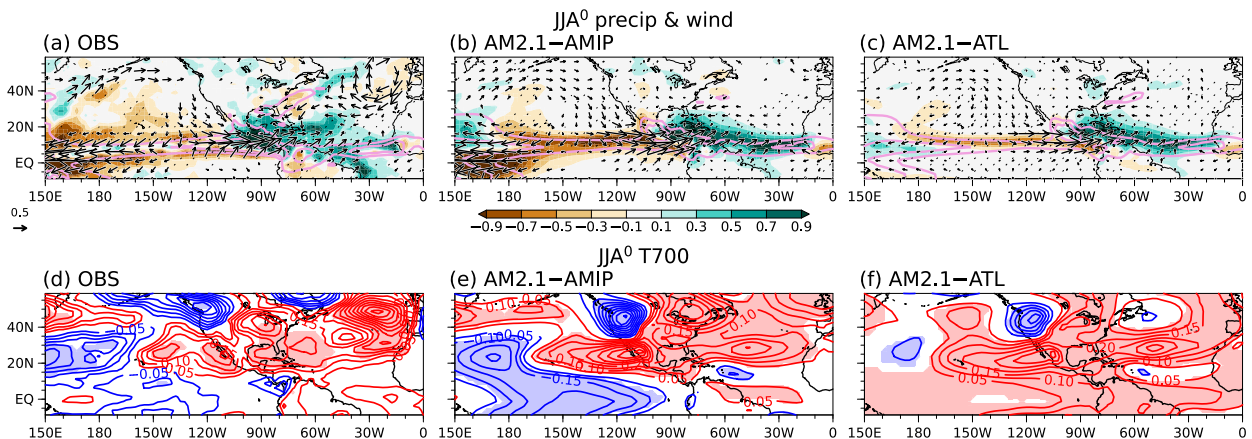

FIG. 8. JJA^0 partial regression coefficients onto the MAM^0 NTA index in (a),(d) observations, (b),(e) AM2.1-AMIP, and (c),(f) AM2.1-ATL. (a)–(c) Precipitation (mm day^{-1}; color shading) and surface winds (m s^{-1}; arrows; only points with the 90% confidence are drawn). Superimposed with purple lines are climatological-mean precipitation (5 and 10 mm day^{-1}). Stippling signifies the 90% confidence for the color-shaded variables. (d)–(f) The 700-hPa temperature (contoured for every 0.05 K with zero lines omitted; color shading signifies the 90% confidence).
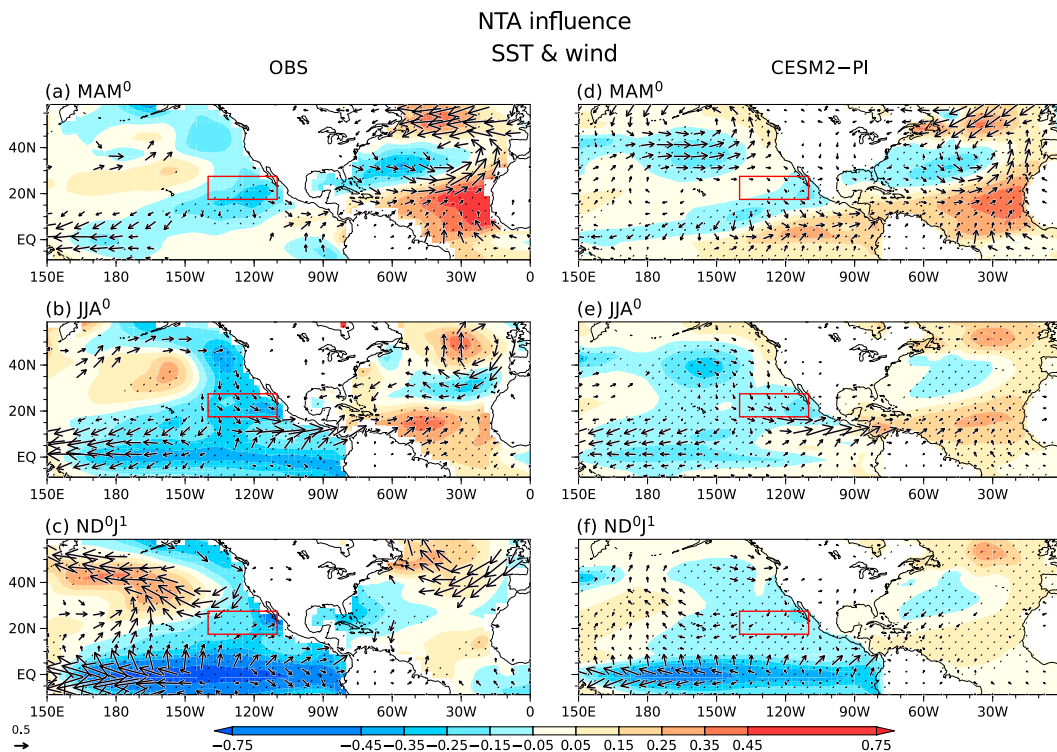
NTA influence
SST & wind

OBS   CESM2−PI

FIG. 9. (a)–(c) Lagged partial regression coefficients of SST (°C; color shading) and surface winds (m s^{-1}; arrows; only points with the 90% confidence are drawn) onto the MAM^0 NTA index in (a) MAM^0, (b) JJA^0, and (c) ND^{0}J^1 in the observations. Stippling indicates the 90% for the color-shaded variables. (d)–(f) As in in (a)–(c), respectively, but for CESM2-PI. The confidence level is set to 99% for CESM2-PI. Red box denotes the NEP box.

Figure 11a shows anomalous LCF and EIS regressed onto residual LCF index, and the corresponding SST and wind anomalies are shown in Fig. 11c. Over the NEP box, the positive LCF anomalies coincide with negative SST and positive EIS anomalies, suggesting positive low cloud–SST feedback. In contrast to the NTA forcing, free-tropospheric warming that exceeds 90% confidence level is limited along the California coast and therefore ineffective in promoting the low cloud–SST feedback through lower-tropospheric stability (Fig. 11e).

A closer inspection reveals that the center of the SST anomalies is slightly shifted northeastward compared with that of the LCF anomalies (Fig. 11c), as identified in Yang et al. (2023). Together with the anomalous northeasterlies (Fig. 11c) across climatological SST gradient (Fig. 1a), this displacement brings cold and dry advection by the climatological northeasterlies (Fig. 1a) in the southern portion of the NEP box. The resultant enhancement of turbulent heat flux promotes SST cooling and low-cloud formation (Klein et al. 1995; Miyamoto et al. 2018).

Figure 12a shows time evolution of SST anomaly and corresponding surface latent heat and radiative fluxes in the NEP box. Low-cloud radiative cooling is mainly responsible for the peak of negative SST anomaly in late summer. This radiative cooling is preceded by statistically significant latent heat flux cooling in winter and early summer. Thus, the latent heat cooling initiates the summertime low cloud–SST feedback.

Although well reproducing the radiative cooling as part of low cloud–SST feedback (Figs. 11b and 12b), CAM6-AMIP fails to capture the evaporative cooling, implying the importance of atmospheric internal variability (Fig. 12b).

Figure 13a shows surface wind anomalies in preceding D^{-1}JF^0. The wintertime latent heat loss is promoted by the anomalous northeasterlies of cold and dry advection (Fig. 13a). The associated SLP anomaly field shown in Fig. 14a features a meridional dipole that resembles the NPO (Walker and Bliss 1932; Rogers 1981). Consistent with the latent heat flux anomalies (Figs. 12a,b), CAM6-AMIP fails to reproduce the NPO anomalies of SLP and wind (Fig. 14b), although it captures weak but statistically significant positive SLP anomalies in the subtropics indicative of the WES feedback (see section 6a). AM2.1-AMIP exhibits almost the same result (Fig. S5). CAM6-AMIP also underestimates anomalous summertime northeasterlies in the NEP box (Figs. 11c,d). These results indicate that the residual LCF variability is dominated by low cloud–SST feedback driven by midlatitude stochastic variability such as the NPO.

6. Discussion

a. Nonlocal low-cloud feedback on NPMM and ENSO

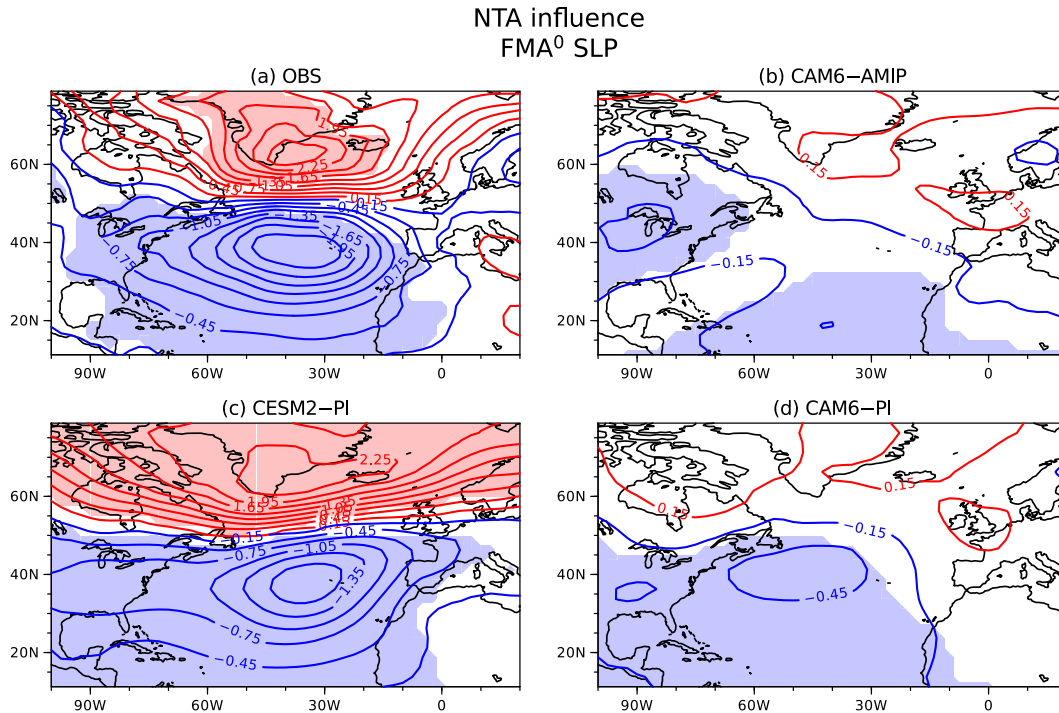Here, we discuss nonlocal low-cloud feedback on the NPMM and subsequent ENSO. Associated with the NTA warming

NTA influence
FMA^0 SLP

FIG. 10. Lagged partial regression of FMA^0 SLP (±0.15, ±0.45, ±0.75, … hPa) onto the MAM^0 NTA index based on (a),(b) observations and (c),(d) CESM2-PI. (a) Observations, (b) CAM6-AMIP, (c) CESM2-PI, and (d) CAM6-PI. Color shading indicates the (a),(b) 90% and (c),(d) 99% confidence.

induced by the stochastic NAO, negative SST anomalies are not only amplified locally by low cloud–SST feedback but also extended southwestward with accelerated trade winds (Figs. 9a,b). This SST and wind pattern resemble the NPMM. Ham et al. (2013) argued that anomalous equatorward winds to the west of the Rossby waves promote latent heat loss from the ocean (as hinted in Fig. 6a) and hence kick off this NPMM-like WES mode. In the low-cloud region, however, we find that the development of the negative SST anomalies in summer involves the low cloud–SST feedback (Fig. 6a). Because dry advection by the climatological northeasterlies (Fig. 1a) and accelerated trade winds (Fig. 9b) promote latent heat loss downstream of the low-cloud region (Miyamoto et al. 2023), increased low clouds act to amplify this NPMM through joint low cloud–WES feedback.

As part of the Rossby wave response to decreased precipitation (Figs. 5g,h), the NPMM is associated with anomalous equatorial easterlies on its southern flank (Fig. 9b). Approaching the equator, these winds kick off the Bjerknes feedback for the development of a La Niña in the subsequent winter (Fig. 9c). Note that the influence of NTA warming on equatorial atmospheric Kelvin waves (Ham and Kug 2015) is weak (Fig. S6) presumably due to the equatorially asymmetric warming. This result suggests the NAO influence on subsequent ENSO through low clouds and NPMM.

The above discussion also applies to the residual LCF variability. The NPO-induced NPMM amplifies through summer due to joint low cloud–WES feedback (Figs. 13b,c). Inducing a Rossby wave response to decreased Pacific ITCZ precipitation

(Figs. 11g,h), the NPMM produces anomalous easterlies along the equator (Fig. 13c) to kick off a La Niña (Fig. 13d). This suggests that the NPO forcing on the NPMM and ENSO (Chiang and Vimont 2004; Zhang et al. 2021, 2022) is reinforced by low-cloud feedback.

b. Support from CESM2 coupled simulation

The observational analysis has revealed that the stochastic NAO and NPO can drive low-cloud variations over the NEP. As CAM6, the atmospheric component of CESM2, shows good skills in simulating NEP low-cloud variations (Figs. 1c and 5), we repeat the same analysis with the 500-yr CESM2-PI to augment the observational analysis.

Partial regression onto the MAM^0 NTA index reveals the NTA influence in CESM2-PI. Figures 9d–f show maps of SST and wind anomalies in CESM2-PI, and corresponding time evolution of anomalous radiative and latent heat flux in the NEP box is shown in Fig. 6c. As in observations, the spring NTA warming is accompanied by weakened trade winds (Fig. 9d) of the negative phase NAO (Fig. 10c). The inability of CAM6-PI forced with CESM2-PI SST to produce the NAO phase implies its stochastic nature (Fig. 10d). The NTA warming excites the warm Rossby waves extending westward accompanied by equatorward winds that promote latent cooling over the NEP (Figs. 6c and 9d,e). As shown in Figs. 7c and 15, these Rossby waves are also accompanied by deep free-tropospheric warming. Both the SST cooling and free-tropospheric warming enhance lower-tropospheric stability and low clouds in the NEP, resulting in radiative cooling that exceeds the latent heat cooling in
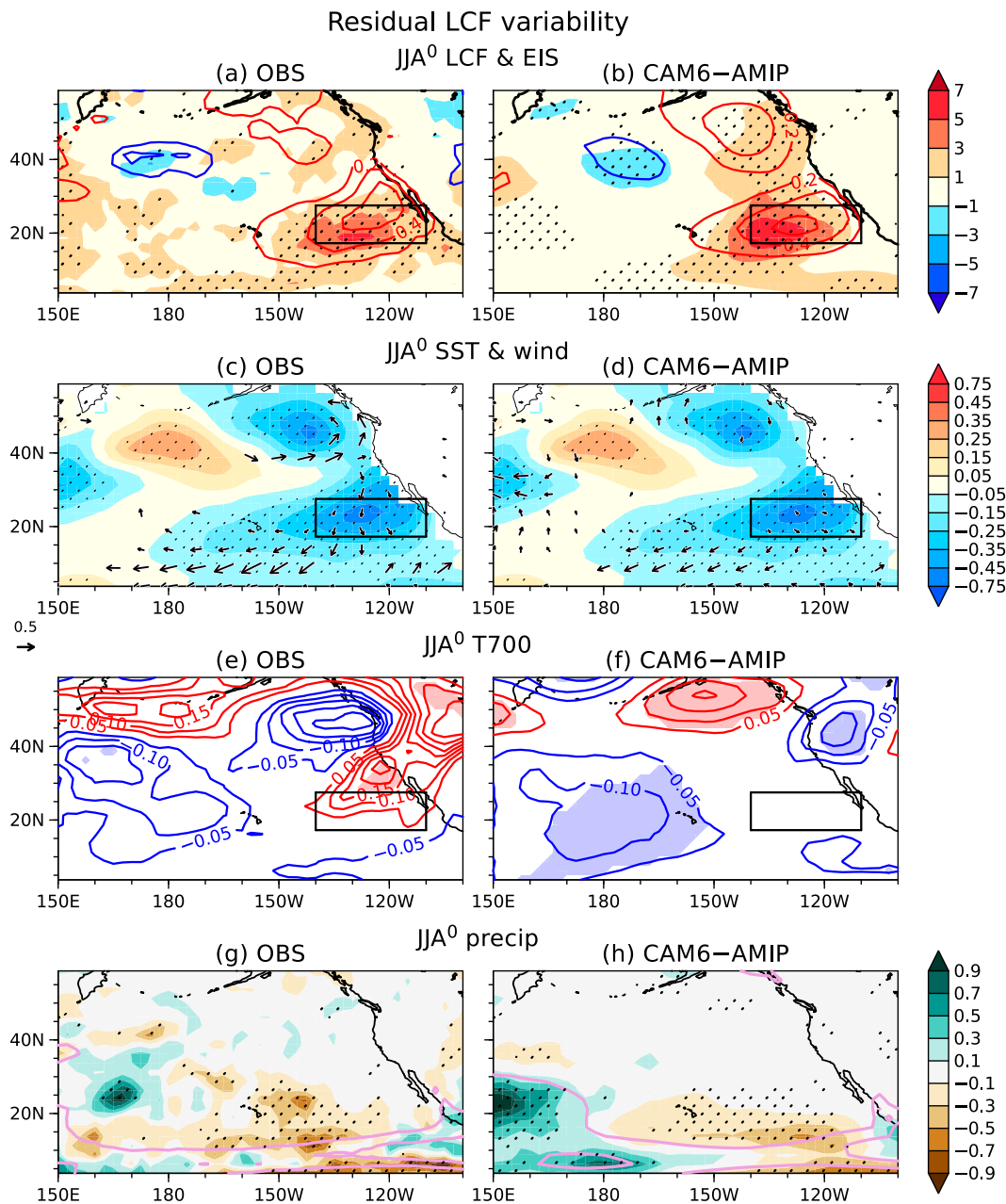
Residual LCF variability

Fig. 11. JJA^0 simple regression coefficients onto the residual MODIS LCF index in (a),(c),(e),(g) observations and (b),(d),(f),(h) CAM6-AMIP. (a),(b) LCF (%; color shading) and EIS (contoured from every 0.2 K with zero lines omitted). (c),(d) SST (°C; color shading) and surface winds (m s^{-1}; arrows; only points with the 90% confidence are drawn). (e),(f) The 700-hPa temperature (contoured for every 0.05 K with zero lines omitted; color shading signifies the 90% confidence). (g),(h) Precipitation (mm day^{-1}; color shading). Superimposed with purple lines are climatological-mean precipitation (5 and 10 mm day^{-1}). Except for (e) and (f), stippling signifies the 90% confidence for the color-shaded variables. Black box denotes the NEP box.

summer (Fig. 6c). These results corroborate the stochastic NAO forcing of NEP low-cloud variability via the NTA SST.

Simple regression onto the residual JJA LCF index in CESM2-PI unveils the NPO-forced low-cloud variations. Figure 12c shows time evolution of SST in the NEP box along with radiative and latent heat flux in CESM2-PI, and corresponding maps of SST and

wind anomalies are shown in Figs. 13e–h. Positive LCF anomaly in the NEP box is accompanied by the negative SST anomaly that develops continuously from winter through spring (Fig. 12c). This SST cooling is initiated by the latent heat cooling in winter and spring (Fig. 12c). Maps of wind anomalies reveal that cold and dry advection by anomalous northerlies
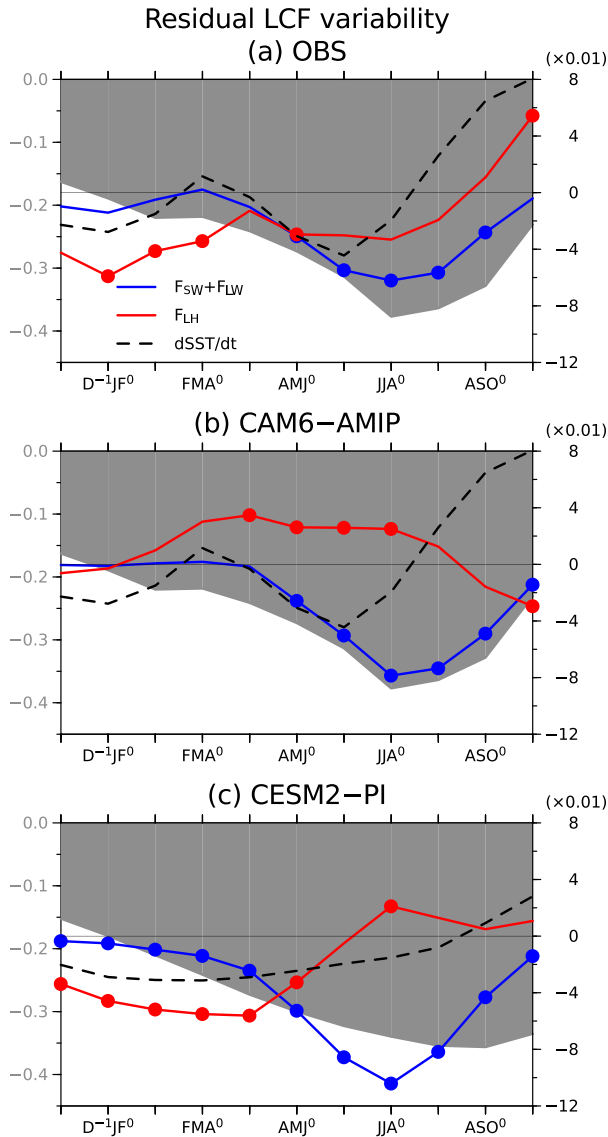
Residual LCF variability
(a) OBS

(b) CAM6−AMIP

(c) CESM2−PI

FIG. 12. Lagged regression of surface radiation and latent heat flux onto the JJA^0 residual MODIS LCF index. The 3-month-mean simple regression coefficients of $F'_{SW+LW}/\rho c_p \overline{H}$ (blue) and $F'_{LH}/\rho c_p \overline{H}$ (red) in the NEP box (black and red boxes in Figs. 11 and 13) onto the residual LCF variability in (a) observations, (b) CAM6-AMIP, and (c) CESM2-PI. Unit is °C (30 day)$^{-1}$ with reference on the right axis. Dot signifies the 90% and 99% confidence for (a), (b), and (c), respectively. Gray filled line indicates the corresponding regression of SST (°C; reference on the left axis) and its time derivative [°C (30 day)$^{-1}$] averaged over the NEP box, respectively, in (a) and (b) observations and (c) CESM2-PI.

causes this latent heat cooling (Figs. 13e,f). As shown in Fig. 14c, the associated SLP pattern resembles the NPO in winter and similarly in spring (not shown). CAM6-PI forced with CESM2-PI SST fails to reproduce the NPO (Fig. 14d), suggesting the importance of atmospheric internal variability. Low cloud–SST feedback amplifies the NEP SST anomaly after the NPO forcing weakens (Figs. 12c and 13g). Although

the spring NPO forcing is stronger in CESM2-PI than in observations, these results corroborate the stochastic NPO forcing.

Forced by the NPO and NAO, the NPMM-like pattern extends southwestward under the climatological northeasterlies and WES feedback (Figs. 9d,e and 13f,g). This NPMM induces anomalous equatorial easterlies (Figs. 9e and 13g), promoting a La Niña in the subsequent winter through the Bjerknes feedback (Figs. 9f and 13h). As in Fig. S4, partial regression onto the FMA^0 NAO index supports the NAO forcing (Fig. S7), albeit the statistical significance in the observations weakens due to noise. These results suggest that the NAO and NPO stochastically drive the joint low cloud–WES mode and subsequent ENSO as in the observations.

7. Summary

The NPMM receives renewed interest as a key conduit for extratropical atmospheric variability to affect tropical climate. While the WES feedback has long been identified as important for its southwestward propagation into the central Pacific, recent modeling studies highlighted the role of low-cloud feedback in amplifying and sustaining the NPMM through summer (Bellomo et al. 2014; Middlemas et al. 2019; Yang et al. 2023; Miyamoto et al. 2023). The present study has investigated the summertime interannual variations of the NEP low clouds and their mechanisms. By using multiple linear regression, we have identified that winter NPO and NAO modes of atmospheric internal variability drive low-cloud variability over the NEP. The NPO directly affects the NEP SST and hence low clouds, whereas the NAO modulates the NTA SST and remotely affects the NEP low clouds through baroclinic Rossby waves (schematic in Fig. 16). The CESM2 preindustrial control simulation corroborates our results.

Partial regression onto spring NTA SST reveals that the NTA warming by the stochastic NAO promotes the NEP low cloud–SST feedback. Enhanced deep convection over the anomalously warm NTA excites warm Rossby waves that extend into NEP. The resultant enhancement of static stability promotes low cloud–SST covariability. The NEP SST anomalies amplified by the low cloud–SST feedback extend southwestward with the help of the climatological winds and WES feedback, consistent with the NPMM-like nonlocal effects of low clouds identified by recent modeling studies. The associated equatorial wind anomalies modulate the subsequent evolution of ENSO. This study for the first time reveals the stochastic NAO influence on the NEP low cloud–SST feedback via the NTA SST.

Regressing out the effects of the preceding ENSO and NTA SST unveils the winter NPO forcing on NEP low clouds. Anticyclonic wind anomalies associated with the NPO promote NEP cooling by latent heat loss and through low cloud–SST feedback. The AMIP simulation fails to reproduce the NPO forcing, suggestive of the atmospheric internal variability. The NPO forcing of the NPMM is consistent with previous studies (Chiang and Vimont 2004; Zhang et al. 2021, 2022), but this study highlights the overlooked low cloud–SST feedback.

Although previous studies pointed out the NTA influence on the NPMM and ENSO, this study suggests that the NEP
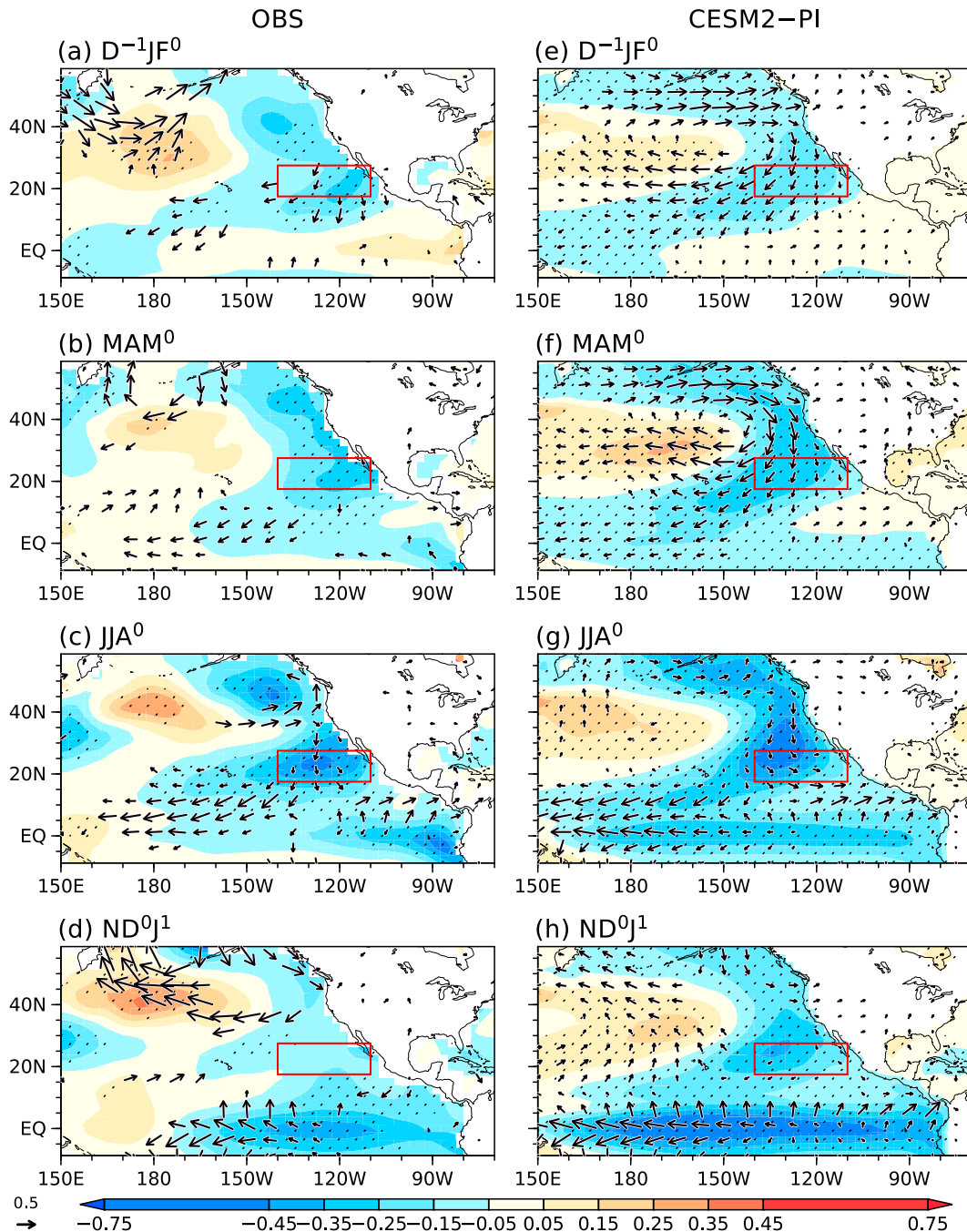
Residual LCF variability
SST & wind

OBS

(a) $D^{-1}JF^0$

(b) MAM^0

(c) JJA^0

(d) ND^0J^1

CESM2−PI

(e) $D^{-1}JF^0$

(f) MAM^0

(g) JJA^0

(h) ND^0J^1

0.5 →
−0.75 −0.45 −0.35 −0.25 −0.15 −0.05 0.05 0.15 0.25 0.35 0.45 0.75

FIG. 13. (a)–(c) Lagged simple regression coefficients of SST (°C; color shading) and surface winds (m s^{-1}; arrows; only points with the 90% confidence are drawn) onto JJA^0 MODIS residual LCF index in (a) MAM^0, (b) JJA^0, and (c) ND^0J^1. Stippling indicates the 90% for the color-shaded variables. (d)–(f) As in (a)–(c), respectively, but for CESM2-PI. The confidence level is set to 99% for CESM2-PI. Red box denotes the NEP box.

low cloud–SST feedback is a key conduit for this NTA influence. Although regressed out in our analysis, the preceding El Niño can also generate NTA warming (Alexander et al. 2002), which partially offsets the ENSO-induced low-cloud

and NPMM anomalies. Despite the importance of the transbasin interactions, global climate models tend to underestimate the NTA influence on the ENSO through the subtropical pathway (Ham and Kug 2015; Yang et al. 2022). As most climate
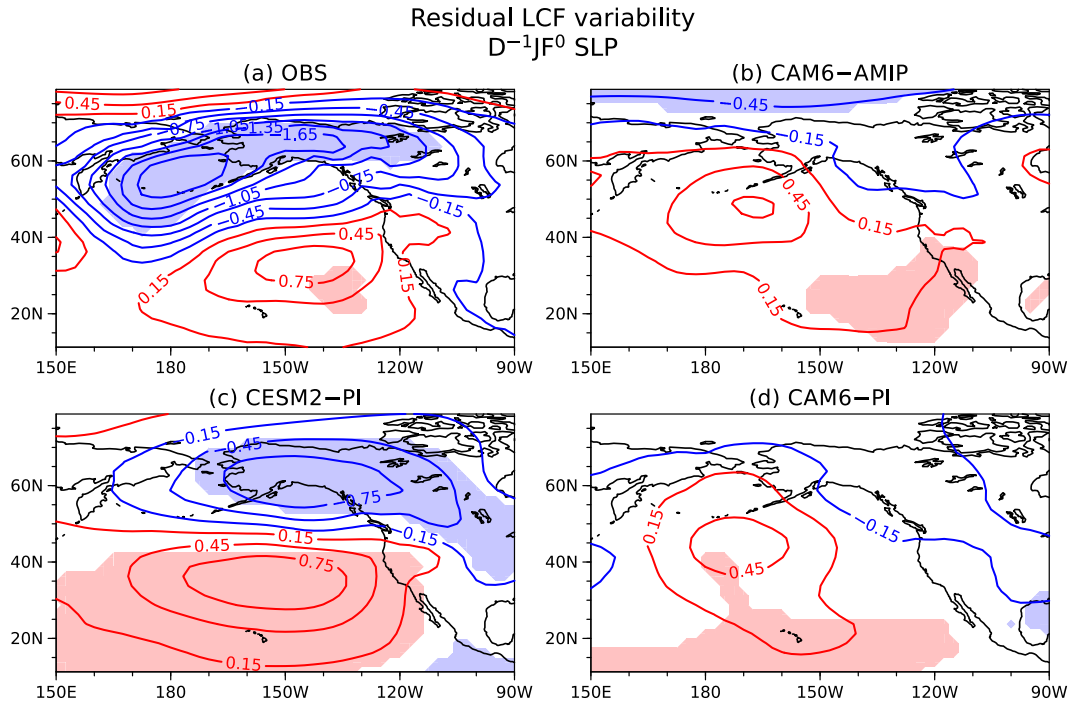
Residual LCF variability
$D^{-1}JF^0$ SLP

FIG. 14. Lagged simple regression coefficients of $D^{-1}JF^0$ SLP (± 0.15, ± 0.45, ± 0.75, … hPa) onto the JJA^0 residual LCF index based on (a),(b) observations and (c),(d) CESM2-PI. (a) Observations, (b) CAM6-AMIP, (c) CESM2-PI, and (d) CAM6-PI. Color shading indicates the (a),(b) 90% and (c),(d) 99% confidence.

models have difficulty in realistically simulating low-cloud variability (e.g., Myers et al. 2018), the present study implies that low-cloud response to NTA SST may be the key to reproducing the Atlantic forcing on the Pacific. This will be pursued in future work.

In addition to the preceding ENSO effect (Yang et al. 2023), removing the Atlantic contribution is crucial in isolating the North Pacific stochastic forcing on low cloud–SST covariability. Based on the residual variability of the multiple linear regression, we have successfully extracted the NPO

FIG. 15. Partial regression of JJA^0 precipitation (mm day^{-1}; color shading) and 700-hPa temperature (contoured in red for 0.1 and 0.2 K) onto the MAM^0 NTA index in CESM2-PI. Superimposed with purple lines are climatological-mean precipitation (5 and 10 mm day^{-1}). Stippling indicates the 99% confidence of precipitation anomaly. Light blue line in (g) and (h) indicates cross section in Fig. 7.

forcing on the joint low cloud–WES mode that triggers the ENSO. Although a targeted coupled model experiment is an important future challenge, such a framework is useful to disentangle the effect of ENSO remnants, Atlantic influence, and midlatitude stochastic variability on the joint low cloud–WES feedback.

Finally, the short record of satellite observations limits our ability to identify the effects of ENSO asymmetry and diversity. It also hinders the investigation of decadal variations of the low clouds (e.g., Clement et al. 2009). For example, the Atlantic multidecadal oscillation (e.g., Deser et al. 2010) has been proposed to affect the NPMM and equatorial Pacific (Yu et al. 2015). Background warming of NTA and associated enhanced precipitation variations (Ding et al. 2023) may amplify the interannual NTA influence on low clouds. Along
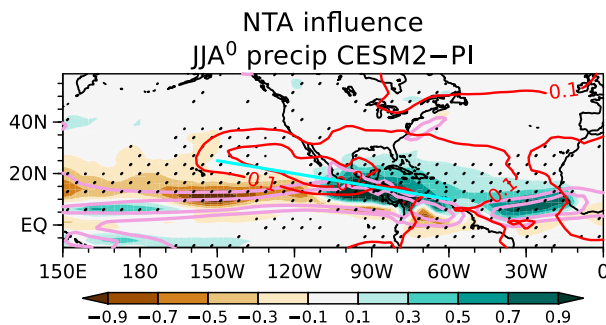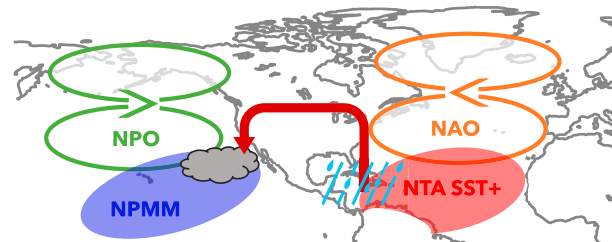

FIG. 16. Schematic of the NPO and NAO forcing on NEP low clouds (gray object) identified in the present study. The red block arrow indicates the vertical circulation associated with enhanced deep convection over the NTA warming.

with climate model simulations, long historical observations, such as those from ships, can give further insights into the roles of low clouds in climate variability and change.

Data availability statement. The observational data used in this study are available online (ERA5: https://cds.climate. copernicus.eu; CERES-EBAF: https://ceres.larc.nasa.gov/data; ERSST: https://www.ncei.noaa.gov/products/extended-reconst ructed-sst; MILA-GPV: https://www.jamstec.go.jp/argo_research/ dataset/milagpv/mila_en.html; GPCP: https://disc.gsfc.nasa.gov/ datasets/GPCPMON_3.2/summary; MODIS: https://ladsweb. modaps.eosdis.nasa.gov/archive/allData/61/MOD08_D3; OAFlux: http://rda.ucar.edu/datasets/ds260.1/). CAM6 and CESM2 simulations were downloaded from the Casper system in National Center for Atmospheric Research. The authors can provide GFDL AM2.1 experiments upon reasonable requests.

REFERENCES

Alexander, M. A., I. Bladé, M. Newman, J. R. Lanzante, N.-C. Lau, and J. D. Scott, 2002: The atmospheric bridge: The influence of ENSO teleconnections on air–sea interaction over the global oceans. *J. Climate*, **15**, 2205–2231, https://doi.org/ 10.1175/1520-0442(2002)015<2205:TABTIO>2.0.CO;2.

Amaya, D. J., 2019: The Pacific Meridional Mode and ENSO: A review. *Curr. Climate Change Rep.*, **5**, 296–307, https://doi. org/10.1007/s40641-019-00142-x.

Bellomo, K., A. Clement, T. Mauritsen, G. Rädel, and B. Stevens, 2014: Simulating the role of subtropical stratocumulus clouds in driving Pacific climate variability. *J. Climate*, **27**, 5119–5131, https://doi.org/10.1175/JCLI-D-13-00548.1.

Bjerknes, J., 1969: Atmospheric teleconnections from the equatorial Pacific. *Mon. Wea. Rev.*, **97**, 163–172, https://doi.org/10. 1175/1520-0493(1969)097<0163:ATFTEP>2.3.CO;2.

Chang, P., L. Ji, and R. Saravanan, 2001: A hybrid coupled model study of tropical Atlantic variability. *J. Climate*, **14**, 361–390, https://doi.org/10.1175/1520-0442(2001)013<0361:AHCMSO> 2.0.CO;2.

——, L. Zhang, R. Saravanan, D. J. Vimont, J. C. H. Chiang, L. Ji, H. Seidel, and M. K. Tippett, 2007: Pacific meridional mode and El Niño—Southern Oscillation. *Geophys. Res. Lett.*, **34**, L16608, https://doi.org/10.1029/2007GL030302.

Chiang, J. C. H., and D. J. Vimont, 2004: Analogous Pacific and Atlantic meridional modes of tropical atmosphere–ocean variability. *J. Climate*, **17**, 4143–4158, https://doi.org/10.1175/ JCLI4953.1.

Clement, A. C., R. Burgman, and J. R. Norris, 2009: Observational and model evidence for positive low-level cloud feedback. *Science*, **325**, 460–464, https://doi.org/10.1126/science. 1171255.

Danabasoglu, G., and Coauthors, 2020: The Community Earth System Model Version 2 (CESM2). *J. Adv. Model. Earth Syst.*, **12**, e2019MS001916, https://doi.org/10.1029/2019MS001916.

Deser, C., M. A. Alexander, S.-P. Xie, and A. S. Phillips, 2010: Sea surface temperature variability: Patterns and mechanisms. *Annu. Rev. Mar. Sci.*, **2**, 115–143, https://doi.org/10. 1146/annurev-marine-120408-151453.

Ding, R., and Coauthors, 2023: North Atlantic Oscillation controls multidecadal changes in the North Tropical Atlantic–Pacific connection. *Nat. Commun.*, **14**, 862, https://doi.org/10.1038/ s41467-023-36564-3.

Du, Y., and S.-P. Xie, 2008: Role of atmospheric adjustments in the tropical Indian Ocean warming during the 20th century in climate models. *Geophys. Res. Lett.*, **35**, L08712, https:// doi.org/10.1029/2008GL033631.

Eyring, V., S. Bony, G. A. Meehl, C. A. Senior, B. Stevens, R. J. Stouffer, and K. E. Taylor, 2016: Overview of the Coupled Model Intercomparison Project phase 6 (CMIP6) experimental design and organization. *Geosci. Model Dev.*, **9**, 1937–1958, https://doi.org/10.5194/gmd-9-1937-2016.

GFDL Global Atmospheric Model Development Team, 2004: The new GFDL global atmosphere and land model AM2–LM2: Evaluation with prescribed SST simulations. *J. Climate*, **17**, 4641–4673, https://doi.org/10.1175/JCLI-3223.1.

Gill, A. E., 1980: Some simple solutions for heat-induced tropical circulation. *Quart. J. Roy. Meteor. Soc.*, **106**, 447–462, https:// doi.org/10.1002/qj.49710644905.

Ham, Y.-G., and J.-S. Kug, 2015: Role of North Tropical Atlantic SST on the ENSO simulated using CMIP3 and CMIP5 models. *Climate Dyn.*, **45**, 3103–3117, https://doi.org/10.1007/ s00382-015-2527-z.

——, ——, J.-Y. Park, and F.-F. Jin, 2013: Sea surface temperature in the north tropical Atlantic as a trigger for El Niño/ Southern Oscillation events. *Nat. Geosci.*, **6**, 112–116, https:// doi.org/10.1038/ngeo1686.

Hartmann, D. L., and D. A. Short, 1980: On the use of Earth radiation budget statistics for studies of clouds and climate. *J. Atmos. Sci.*, **37**, 1233–1250, https://doi.org/10.1175/1520-0469 (1980)037<1233:OTUOER>2.0.CO;2.

Hersbach, H., and Coauthors, 2020: The ERA5 global reanalysis. *Quart. J. Roy. Meteor. Soc.*, **146**, 1999–2049, https://doi.org/10. 1002/qj.3803.

Hosoda, S., T. Ohira, K. Sato, and T. Suga, 2010: Improved description of global mixed-layer depth using Argo profiling floats. *J. Oceanogr.*, **66**, 773–787, https://doi.org/10.1007/s10872-010-0063-3.

Huang, B., and Coauthors, 2017: Extended Reconstructed Sea Surface Temperature, version 5 (ERSSTv5): Upgrades, validations, and intercomparisons. *J. Climate*, **30**, 8179–8205, https://doi.org/10.1175/JCLI-D-16-0836.1.

Huffman, G. J., R. F. Adler, A. Behrangi, D. T. Bolvin, E. J. Nelkin, G. Gu, and M. R. Ehsani, 2023: The new version 3.2 Global Precipitation Climatology Project (GPCP) monthly and daily precipitation products. *J. Climate*, **36**, 7635–7655, https://doi.org/ 10.1175/JCLI-D-23-0123.1.

Kato, S., and Coauthors, 2018: Surface irradiances of edition 4.0 Clouds and the Earth's Radiant Energy System (CERES) Energy Balanced and Filled (EBAF) data product. *J. Climate*, **31**, 4501–4527, https://doi.org/10.1175/JCLI-D-17-0523.1.

Klein, S. A., and D. L. Hartmann, 1993: The seasonal cycle of low stratiform clouds. *J. Climate*, **6**, 1587–1606, https://doi.org/10.1175/1520-0442(1993)006%3C1587:TSCOLS%3E2.0.CO;2.

——, ——, and J. R. Norris, 1995: On the relationships among low-cloud structure, sea surface temperature, and atmospheric circulation in the summertime northeast Pacific. *J. Climate*, **8**, 1140–1155, https://doi.org/10.1175/1520-0442(1995)008<1140:OTRALC>2.0.CO;2.

Koshiro, T., and M. Shiotani, 2014: Relationship between low stratiform cloud amount and estimated inversion strength in the lower troposphere over the global ocean in terms of cloud types. *J. Meteor. Soc. Japan*, **92**, 107–120, https://doi.org/10.2151/jmsj.2014-107.

Kug, J.-S., J. Vialard, Y.-G. Ham, J.-Y. Yu, and M. Lengaigne, 2020: ENSO remote forcing: Influence of climate variability outside the tropical Pacific. *El Niño Southern Oscillation in a Changing Climate*, *Geophys. Monogr.*, Vol. 253, Amer. Geophys. Union, 249–265, https://doi.org/10.1002/9781119548164.ch11.

Loeb, N. G., and Coauthors, 2018: Clouds and the Earth's Radiant Energy System (CERES) Energy Balanced and Filled (EBAF) top-of-atmosphere (TOA) edition-4.0 data product. *J. Climate*, **31**, 895–918, https://doi.org/10.1175/JCLI-D-17-0208.1.

Luongo, M. T., S.-P. Xie, I. Eisenman, Y.-T. Hwang, and H.-Y. Tseng, 2023: A pathway for Northern Hemisphere extratropical cooling to elicit a tropical response. *Geophys. Res. Lett.*, **50**, e2022GL100719, https://doi.org/10.1029/2022GL100719.

Ma, J., S.-P. Xie, and H. Xu, 2017: Contributions of the North Pacific meridional mode to ensemble spread of ENSO prediction. *J. Climate*, **30**, 9167–9181, https://doi.org/10.1175/JCLI-D-17-0182.1.

——, ——, ——, J. Zhao, and L. Zhang, 2021: Cross-basin interactions between the tropical Atlantic and Pacific in the ECMWF hindcasts. *J. Climate*, **34**, 2459–2472, https://doi.org/10.1175/JCLI-D-20-0140.1.

Matsuno, T., 1966: Quasi-geostrophic motions in the equatorial area. *J. Meteor. Soc. Japan*, **44**, 25–43, https://doi.org/10.2151/jmsj1965.44.1_25.

Metz, W., 1991: Optimal relationship of large-scale flow patterns and the barotropic feedback due to high-frequency eddies. *J. Atmos. Sci.*, **48**, 1141–1159, https://doi.org/10.1175/1520-0469(1991)048%3C1141:OROLSF%3E2.0.CO;2.

Middlemas, E., A. Clement, and B. Medeiros, 2019: Contributions of atmospheric and oceanic feedbacks to subtropical northeastern sea surface temperature variability. *Climate Dyn.*, **53**, 6877–6890, https://doi.org/10.1007/s00382-019-04964-1.

Miyamoto, A., H. Nakamura, and T. Miyasaka, 2018: Influence of the subtropical high and storm track on low-cloud fraction and its seasonality over the south Indian Ocean. *J. Climate*, **31**, 4017–4039, https://doi.org/10.1175/JCLI-D-17-0229.1.

——, ——, S.-P. Xie, T. Miyasaka, and Y. Kosaka, 2023: Radiative impacts of Californian marine low clouds on North Pacific climate in a global climate model. *J. Climate*, **36**, 8443–8459, https://doi.org/10.1175/JCLI-D-23-0153.1.

Mori, M., Y. Kosaka, B. Taguchi, H. Tokinaga, H. Tatebe, and H. Nakamura, 2024: Northern Hemisphere winter atmospheric teleconnections are intensified by extratropical ocean-atmosphere coupling. *Commun. Earth Environ.*, **5**, 124, https://doi.org/10.1038/s43247-024-01282-1.

Myers, T. A., and C. R. Mechoso, 2020: Relative contributions of atmospheric, oceanic, and coupled processes to North Pacific and North Atlantic variability. *Geophys. Res. Lett.*, **47**, e2019GL086321, https://doi.org/10.1029/2019GL086321.

——, ——, and M. J. DeFlorio, 2018: Coupling between marine boundary layer clouds and summer-to-summer sea surface temperature variability over the North Atlantic and Pacific. *Climate Dyn.*, **50**, 955–969, https://doi.org/10.1007/s00382-017-3651-8.

Norris, J. R., 2005: Multidecadal changes in near-global cloud cover and estimated cloud cover radiative forcing. *J. Geophys. Res.*, **110**, D08206, https://doi.org/10.1029/2004JD005600.

——, and C. B. Leovy, 1994: Interannual variability in stratiform cloudiness and sea surface temperature. *J. Climate*, **7**, 1915–1925, https://doi.org/10.1175/1520-0442(1994)007<1915:IVISCA>2.0.CO;2.

——, Y. Zhang, and J. M. Wallace, 1998: Role of low clouds in summertime atmosphere–ocean interactions over the North Pacific. *J. Climate*, **11**, 2482–2490, https://doi.org/10.1175/1520-0442(1998)011%3C2482:ROLCIS%3E2.0.CO;2.

Okumura, Y. M., and C. Deser, 2010: Asymmetry in the duration of El Niño and La Niña. *J. Climate*, **23**, 5826–5843, https://doi.org/10.1175/2010JCLI3592.1.

Platnick, S., P. Hubanks, K. Meyer, and M. D. King, 2015: MODIS Atmosphere L3 daily product. NASA MODIS Adaptive Processing System. Goddard Space Flight Center, accessed 6 January 2022, https://modis.gsfc.nasa.gov/data/dataprod/mod08.php.

Rayner, N. A., D. E. Parker, E. B. Horton, C. K. Folland, L. V. Alexander, D. P. Rowell, E. C. Kent, and A. Kaplan, 2003: Global analyses of sea surface temperature, sea ice, and night marine air temperature since the late nineteenth century. *J. Geophys. Res.*, **108**, 4407, https://doi.org/10.1029/2002JD002670.

Rodríguez-Fonseca, B., Y.-G. Ham, S.-K. Lee, M. Martín-Rey, I. P. Sánchez, and R. R. Rodrigues, 2020: Interacting interannual variability of the Pacific and Atlantic oceans. *Interaction Climates of Ocean Basins Observations, Mechanisms, Predictability, and Impacts*, C. R. Mechoso, Ed., Cambridge University Press, 120–152, https://doi.org/10.1017/9781108610995.005.

Rogers, J. C., 1981: The North Pacific oscillation. *J. Climatol.*, **1**, 39–57, https://doi.org/10.1002/joc.3370010106.

Taylor, K. E., R. J. Stouffer, and G. A. Meehl, 2012: An overview of CMIP5 and the experiment design. *Bull. Amer. Meteor. Soc.*, **93**, 485–498, https://doi.org/10.1175/BAMS-D-11-00094.1.

Vimont, D. J., J. M. Wallace, and D. S. Battisti, 2003: The seasonal footprinting mechanism in the Pacific: Implications for ENSO. *J. Climate*, **16**, 2668–2675, https://doi.org/10.1175/1520-0442(2003)016<2668:TSFMIT>2.0.CO;2.

Walker, G. T., and E. W. Bliss, 1932: World weather v. *Mem. Roy. Meteor. Soc.*, **4**, 53–84.

Wallace, J. M., and D. S. Gutzler, 1981: Teleconnections in the geopotential height field during the Northern Hemisphere winter. *Mon. Wea. Rev.*, **109**, 784–812, https://doi.org/10.1175/1520-0493(1981)109%3C0784:TITGHF%3E2.0.CO;2.

Warren, S. G., C. J. Hahn, J. London, R. M. Chervin, and R. L. Jenne, 1988: Global distribution of total cloud cover and cloud type amounts over the ocean. NCAR Tech. Note NCAR/TN-317+STR, 212 pp., https://atmos.uw.edu/CloudMap/Atlases/DistOcean.pdf.

Wood, R., 2012: Stratocumulus clouds. *Mon. Wea. Rev.*, **140**, 2373–2423, https://doi.org/10.1175/MWR-D-11-00121.1.

——, and C. S. Bretherton, 2006: On the relationship between stratiform low cloud cover and lower-tropospheric stability. *J. Climate*, **19**, 6425–6432, https://doi.org/10.1175/JCLI3988.1.

Xie, S.-P., 2024: Subtropical climate: Trade winds and low clouds. *Coupled Atmosphere-Ocean Dynamics: From El Niño to Climate Change*, Elsevier Science, 139–163, https://doi.org/10.1016/C2021-0-02107-6.

——, and S. G. H. Philander, 1994: A coupled ocean-atmosphere model of relevance to the ITCZ in the eastern Pacific. *Tellus*, **46A**, 340–350, https://doi.org/10.3402/tellusa.v46i4.15484.

——, and J. A. Carton, 2004: Tropical Atlantic variability: Patterns, mechanisms, and impacts. *Earth's Climate: The Ocean-Atmosphere Interaction*, Geophys. Monogr., Vol. 147, Amer. Geophys. Union, 121–142, https://doi.org/10.1029/147GM07.

——, C. Deser, G. A. Vecchi, J. Ma, H. Teng, and A. T. Wittenberg, 2010: Global warming pattern formation: Sea surface temperature and rainfall. *J. Climate*, **23**, 966–986, https://doi.org/10.1175/2009JCLI3329.1.

Yang, J.-C., Z. Lv, I. Richter, Y. Zhang, and X. Lin, 2022: Inter-model spread of north tropical Atlantic trans-basin effect substantially biases tropical Pacific Sea surface temperature multiyear prediction. *Geophys. Res. Lett.*, **49**, e2022GL098620, https://doi.org/10.1029/2022GL098620.

Yang, L., S.-P. Xie, S. S. P. Shen, J.-W. Liu, and Y.-T. Hwang, 2023: Low cloud–SST feedback over the subtropical northeast Pacific and the remote effect on ENSO variability. *J. Climate*, **36**, 441–452, https://doi.org/10.1175/JCLI-D-21-0902.1.

Yu, J.-Y., P.-K. Kao, H. Paek, H.-H. Hsu, C.-W. Hung, M.-M. Lu, and S.-I. An, 2015: Linking emergence of the central Pacific El Niño to the Atlantic multidecadal oscillation. *J. Climate*, **28**, 651–662, https://doi.org/10.1175/JCLI-D-14-00347.1.

Yu, L., and R. A. Weller, 2007: Objectively analyzed air–sea heat fluxes for the global ice-free oceans (1981–2005). *Bull. Amer. Meteor. Soc.*, **88**, 527–540, https://doi.org/10.1175/BAMS-88-4-527.

Zhang, Y., and Coauthors, 2021: Pacific meridional modes without equatorial Pacific influence. *J. Climate*, **34**, 5285–5301, https://doi.org/10.1175/JCLI-D-20-0573.1.

——, S.-Y. Yu, D. J. Amaya, Y. Kosaka, M. F. Stuecker, J.-C. Yang, and X. Lin, 2022: Atmospheric forcing of the Pacific Meridional Mode: Tropical Pacific-driven versus internal variability. *Geophys. Res. Lett.*, **49**, e2022GL098148, https://doi.org/10.1029/2022GL098148.